Chapter 5

MnBi/FeNi@C nanocomposites

Chapter 5: MnBi/FeNi@C nanocomposites

5.1. Introduction

In the previous chapter, we observed that cryogenic ball milling is comparatively better than room temperature ball milling for the synthesis of LTP MnBi. Also, exchange-spring magnets help in achieving better magnetic properties. In this context, this chapter deals with the synthesis of FeNi@C nanoparticles via a simple solvothermal route followed by calcination. After structural and magnetic evaluation, this FeNi@C was used as soft-phase for the preparation of exchange–spring magnets with LT MnBi hard phase. Most of the reports on exchange spring magnets, including other REPM hard phases ($Nd_2Fe_{14}B$ and $SmCo_5/Sm_2Co_{17}$), have been exchange coupled with soft phases of α-Fe and $Fe_{65}Co_{35}$ predominantly[1]. These phases are metallic in nature, hence, more susceptible to oxidation, which is detrimental to the overall magnetic properties. Currently, as per the available literature, not much research has been done on using alternative soft materials, like FeNi@C, to develop hard-soft composites, except for work done by Rai et.al on hard–soft $SmCo_5$–FeNi composites [1]. FeNi@C has numerous advantages, including low coercivity (34 Oe), high M_S value (~ 147 emu/g), and the ability to resist oxidation even at elevated temperatures. Assessing FeNi@C as a possible option for the soft phase in nanocomposites is also the aim of this investigation. This study aims to achieve the enhancement of energy product by preparing an exchange spring magnet with LTP MnBi as the hard phase and FeNi@C as the soft magnetic phase. Here, the carbon coating not only would protect the soft phase from oxidation but also has positive effects on the magnetic properties of LTP by facilitating exchange coupling between the phases.

5.2. Results and Discussion

Figure 5.1 refers to the x-ray diffraction pattern obtained from the FeNi@C nanoparticles synthesized from the hydrothermal technique followed by calcination at 700 °C in N_2 environment. The pattern suggests a single-phase formation, corresponding to the FeNi phase, without the presence of any oxides or carbides. This phase has a fcc crystal structure and the corresponding peaks at 43.34, 50 and 74.4 degrees were indexed to be (111), (200) and (222) planes respectively. These sharp crystalline peaks were indexed and matched with the JCPDS file number 47-1417. Further, average crystallite size was calculated taking into consideration the three highest intensity signals from the obtained pattern and using the Scherrer's formula[2]. The calculated average crystallite size value was found to be ~14 nm.

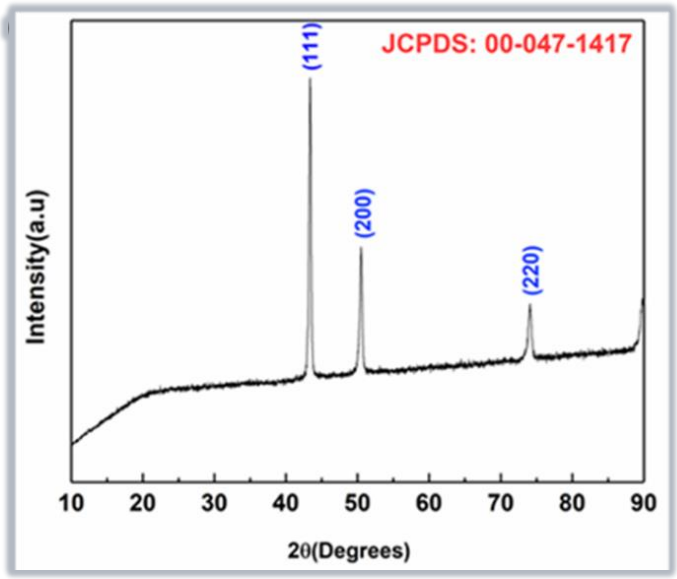

Figure 5.1. X-ray diffraction pattern of FeNi@C nanoparticles.

A hump in the baseline at lower angles i.e., an increase in the slope is evident from 15-30º in figure 1. This feature is often attributed to the poor-crystalline nature of carbon resulting from the break down of its translational symmetry along its radial direction. The

baseline hump where no pure carbon peak can be detected within the given detection limits of the diffractometer is consistent with prior reports [3-4].

Since the desired LTP is a resultant of an incomplete peritectic reaction, Bi and Mn phases are also usually found upon melting. As per literature, to enhance the phase fraction of the desired LTP, homogenization heat treatment at 300 ºC for 24 h was carried out [5,6]. The resultant XRD pattern (Figure 5.2a) also shows Bi and Mn peaks along with the intense LTP peaks. Further, diffraction patterns corresponding to the cryo-milled samples can be seen in Figure 5.2 (b-e).

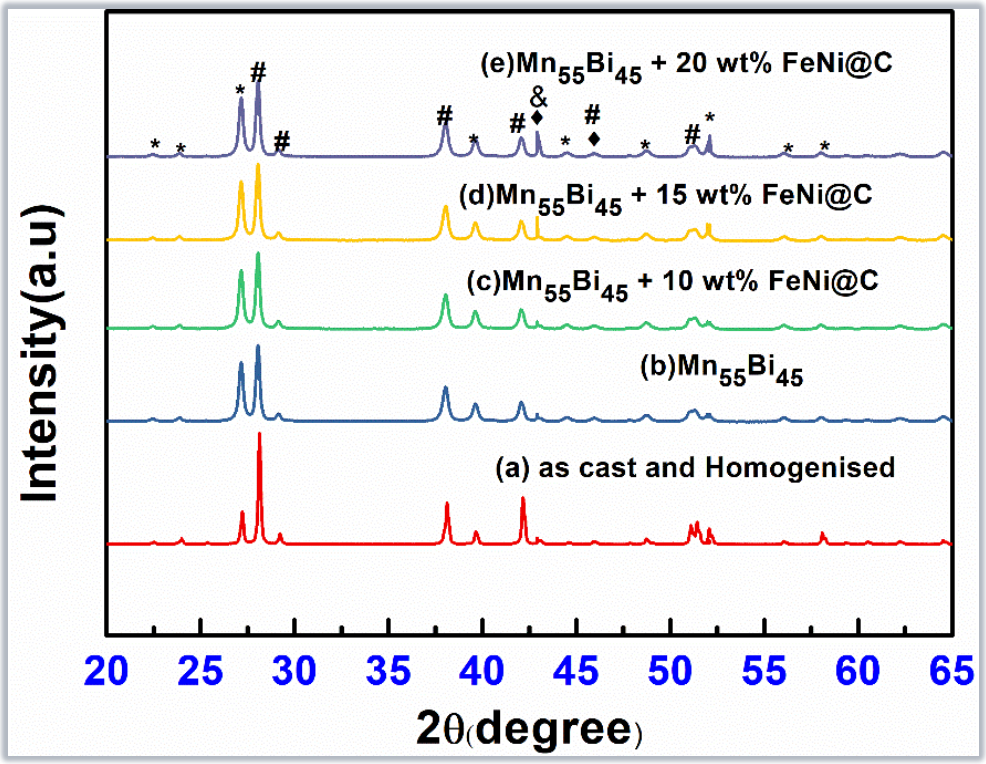

Figure 5.2. X-ray diffraction patterns of (a) $Mn_{55}Bi_{45}$ homogenised powder, $Mn_{55}Bi_{45}$ with (b) 0, (c) 10, (d) 15, and (e) 20 wt. % of FeNi@C after 2 h of cryo-milling. (*-Bi phase, #-LTP MnBi phase, &- FeNi@C, ♦-Mn) ((hkl) indexing is similar to Figure 3.1 and not marked for better comprehensibility).

Due to the particle size reduction associated with milling, these milled samples show peak broadening. According to previous reports, the desirable LTP phase decomposes during the milling process, resulting in an increase in Bi phase [7]. This is indicated by a modest increase in the Bi phase volume fraction of milled samples compared to homogenised sample, which can be observed from the peak intensities. Williamson hall plot was used to calculate the average crystallite size and lattice strain of the cryo-milled $Mn_{55}Bi_{45}$ powder. The average crystallite size for $Mn_{55}Bi_{45}$ powder was found to be around 130 nm whereas the cryo-milled powders with 5, 10, 15, and 20 wt. % of FeNi@C were around 127, 110, 108 and 102 nm respectively.

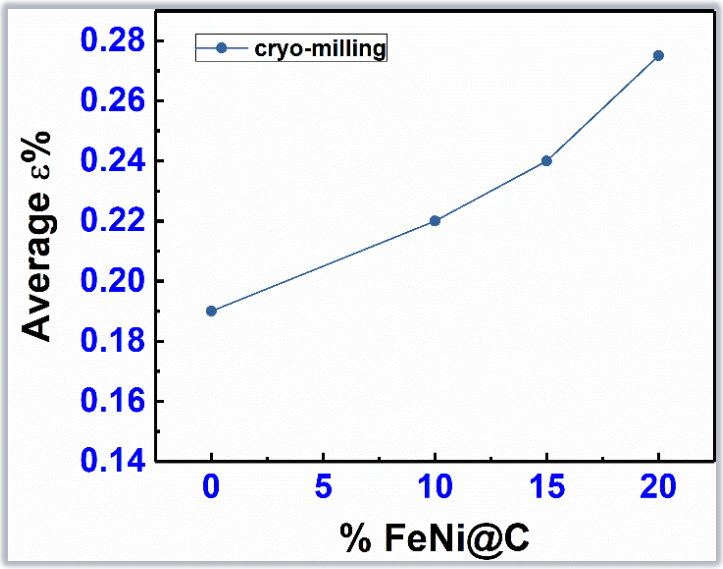

Figure 5.3. Lattice strain variation of cryo-milled $Mn_{55}Bi_{45}$/FeNi@C composites.

The peak broadening with milling also depicts that the lattice strain is caused due to the defects introduced during milling [5,6]. This lattice strain and particle size reduction during ball milling results in the peak broadening as seen in Figure 5.2. The Figure 5.3 shows the variation of lattice strain of cryo-milled powders with FeNi@C addition. Lattice strain is

an important parameter to be considered while milling since it causes decomposition of the desired MnBi phase. For the similar parameters of milling, cryo-milling causes relatively lower lattice strain values [8].

Scanning electron microscopy:

In order to observe the morphology and composition, FeNi@C and nanocomposite of $Mn_{55}Bi_{45}$ with 15 wt.% FeNi@C have been analysed under the secondary electron (SE) and energy dispersive x-ray spectroscopy (EDX) modes of the scanning electron microscope shown as Figure 5.4 and Figure 5.5 respectively.

Figure 5.4 (a-d) depicts the elemental mapping of the constituents of FeNi@C nanoparticles, which confirms an uniform distribution of the elements throughout the sample. The SE micrograph of the nanoparticles show that a larger number of smaller grains are fused to each other due to the high calcination temperature of 700 °C (Figure 5.4e). The EDS spectrum collected from the sample, as shown in Figure 5.4f, corroborates the composition of the nanoparticles.

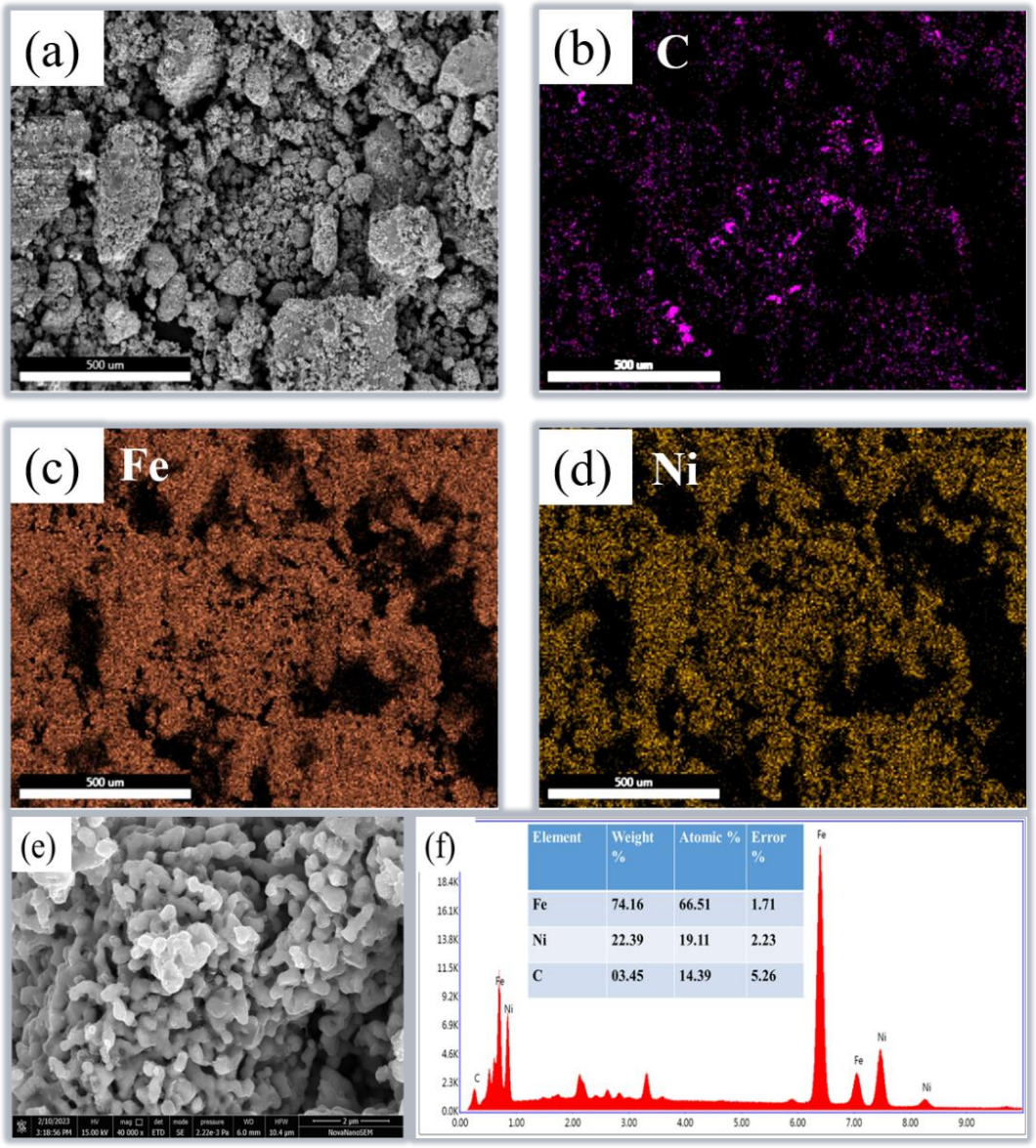

Figure 5.4. (a) Scanning electron micrographs at magnification, elemental mappings of (b) C, (c) Fe, (d) Ni, (e) micrographs at magnification and (f) EDS Spectrum of FeNi@C nanoparticles.

Further figure 5.5a shows the SE micrograph of the randomly shaped nanocomposite of MnBi/FeNi@C after 2 h of cryogenic ball milling. The composition is corroborated by the EDS spectrum showing the corresponding peaks of individual elements (Fig 5.5b). The spectrum shows peaks corresponding to the elements Mn, Bi, Fe, Ni and C. The elemental

mapping of the nanocomposite is also shown in Figure 5.5 (c-g) which displays a homogenous distribution of all the constituents.

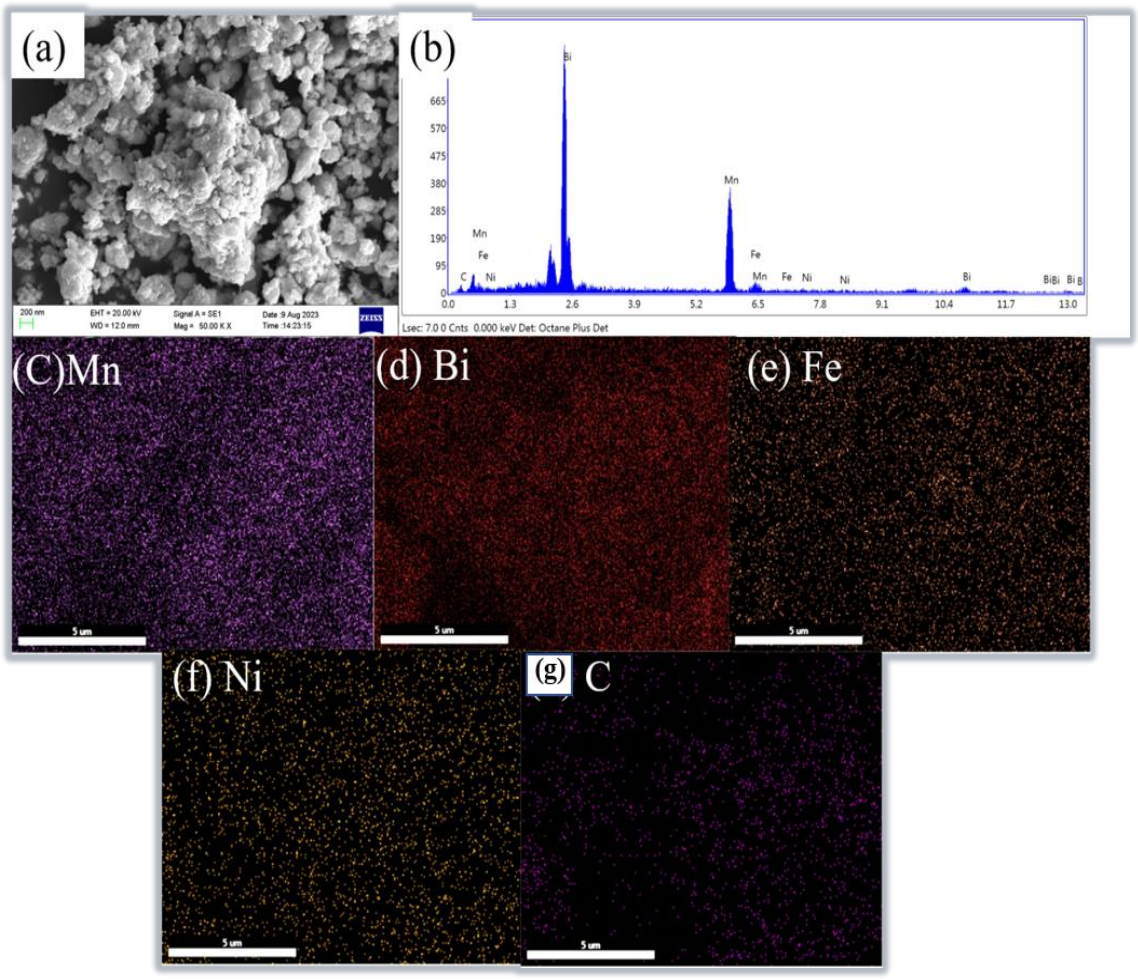

Figure 5.5. (a) Scanning electron micrograph (b) EDS spectrum and the corresponding (c-g) Elemental mapping of all the constituents of cryo-milled MnBi/FeNi@C(15 wt.%) nanocomposite.

Transmission electron microscopy:

The TEM bright field micrograph, figure 5.6a, reveals the FeNi@C microstructure. The apparently bigger grain ~100 nm is consisting of several fused nanograins with a size of 25-35 nm. Certain tube like structures of entirely different contrast, suggesting a material with different morphology can be seen in the Figure 5.6a. Further, Raman Spectroscopy studies were utilized to understand the tube like structures (Figure 5.8).

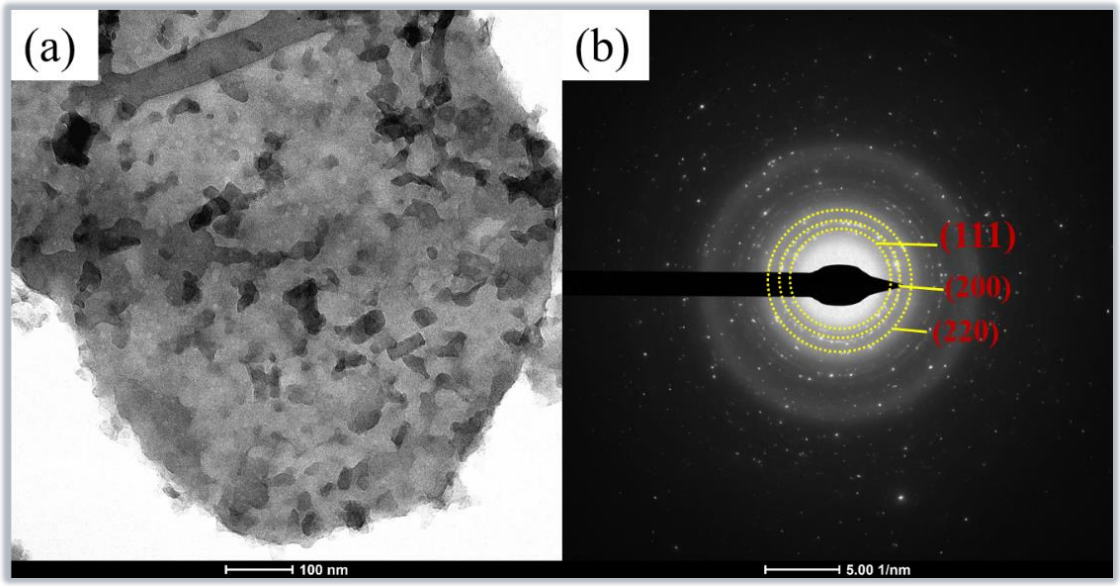

Figure 5.6. (a) Bright-field image and (b) corresponding diffraction pattern of fcc FeNi@C nanoparticles.

The selected area diffraction pattern (Fig 5.6b) collected from the FeNi@C nanoparticles displayed a ring like pattern, suggesting the polycrystalline nature of the sample. The consecutive rings were indexed and were in accordance to the fcc structure and interplanar spacing of the FeNi phase. The (111), (200) and (220) planes can be seen in the indexed SAD pattern, which were found to be in agreement with the interplanar spacing obtained from the XRD pattern (Figure 5.6b).

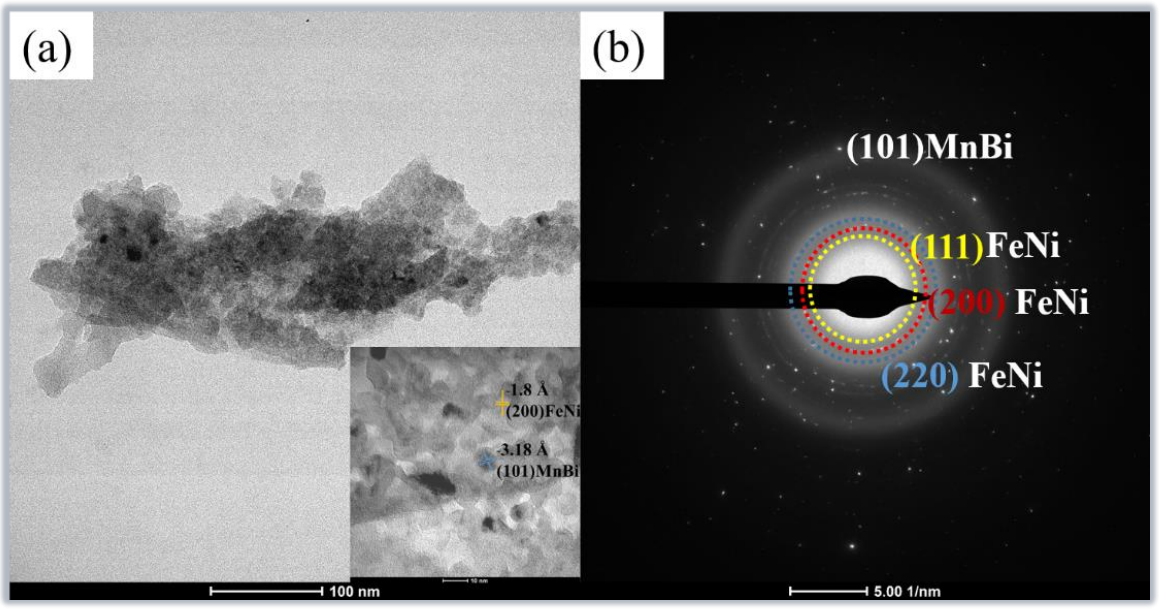

Figure 5.7. Transmission electron micrograph (a) Bright field image (inset showing d-spacing) and (b) corresponding diffraction pattern of nanocomposites of $Mn_{55}Bi_{45}$/ FeNi@C (15 wt.%).

The TEM micrograph of nanocomposite obtained after 2 h of cryomilling of 15 wt.% FeNi@C with $Mn_{55}Bi_{45}$ is shown in Figure 5.7a. The inset of figure 5.7a corresponds to the interplanar spacing of the nanocomposite where d-spacings refer to both the FeNi@C and $Mn_{55}Bi_{45}$ phases. The bright field micrographs show a contrast in colour arising from the different phases of the nanocomposite. The corresponding SAD pattern (Figure 5.7b) along with the insets of figure 5.7a corroborate the presence of both the soft magnetic (FeNi) and hard magnetic (LTP MnBi) phases in the material.

Raman spectroscopy:

The Raman spectra of FeNi@C nanoparticles have been recorded and shown in Figure 5.8. The characteristic first order Raman modes are seen in the frequency range of 1000-2000 cm^{-1}. The large peak at 1345 cm^{-1} has been recognized as the defect generated disorder mode D band [9]. The D mode is commonly observed in sp^2 carbon samples with holes, impurities, and other symmetry-breaking defects. The intensity of the D peak is lower than that of the G peak, indicating that the samples contain only a tiny trace of amorphous carbon (Figure 5.8)[10].

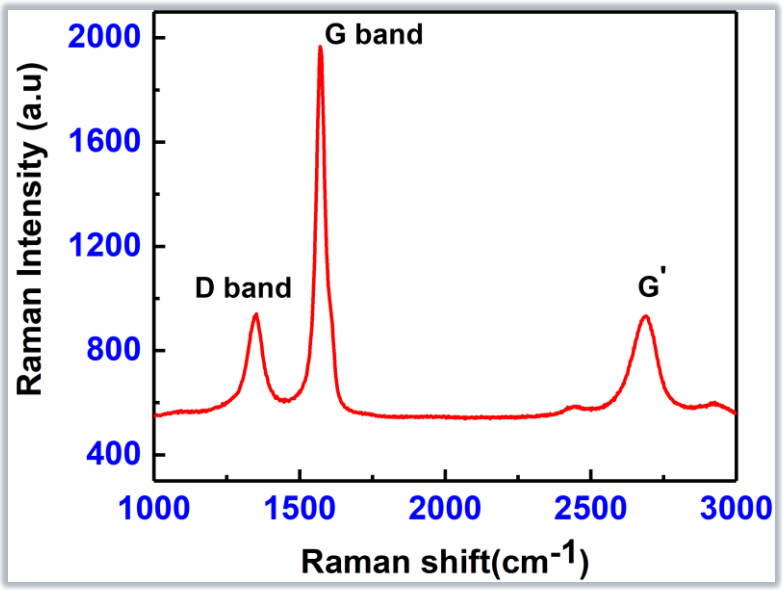

Figure 5.8. High frequency Raman spectrum of FeNi@C nanoparticles.

The E_{2g} mode, also known as the tangential mode or the G peak, is another significant peak detected at 1562 cm^{-1} and is caused by the in-plane vibrational motion of the carbon atoms [11]. The D- and G-bands were visible in the synthesized samples, indicating carbon formation. The peak at 2690 cm^{-1} is classified as a second-order Raman spectrum, and it occurs as an overtone of the D peak. Furthermore, the spectrum in Figure 8 shows a minor

intensity peak at 2916 cm^{-1}. The combination of two powerful Raman modes, the D mode and the high-frequency G+ of the tangential mode, gives rise to these additional higher-order peaks [12]. The significant peak positions and their relative intensities suggest the nature of carbon in FeNi@C would be reduced graphene oxide(r-GO).

Magnetic analysis:

Figure 5.9 illustrates the magnetic behaviour of FeNi@C nanoparticles. The magnetic properties FeNi@C nanoparticles were evaluated at room temperature using a vibrating sample magnetometer with an applied field of ± 5 kOe. The FeNi@C nanoparticles exhibited charecteristic ferromagnetic nature with a saturation magnetization of ~ 147 emu/g, M_r ~ 3.4 emu/g and H_C~ 14 Oe, respectively (Figure 5.9). The M_S value of the nanoparticles is nearby to that of bulk FeNi alloy (~168 $emug^{-1}$) and the coercivity is quite lower than the bulk alloy (~240 Oe) which can be due to numerous reasons [13]. Since a variety of structural factors, including internal stress, orientation, imperfections and shape, can influence the coercivity values [14]. Further, the saturation magnetization of the nanoparticles is remarkably higher than that of $NiFe_2O_4$ precursor particles (~48.1 emu/g). FeNi@C nanoparticles synthesized by various techniques have been reported to show a similar magnetic behaviour with M_S values in the range of 130-150 emu/g [15,16].

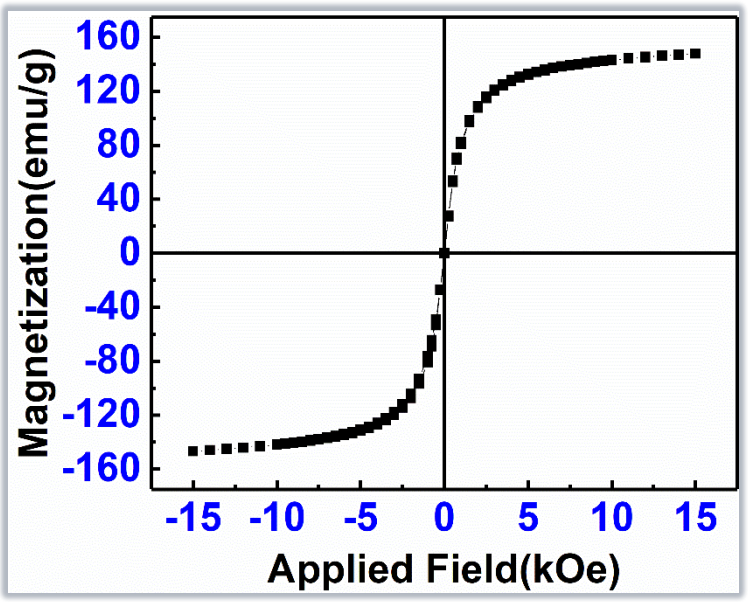

Figure 5.9. Room temperature M *vs*. H hysteresis loops under ± 5 kOe of FeNi nanoparticles.

The magnetic studies performed on the nanocomposites are shown in Figure 5.10. Due to the reduction in particle size with milling, a coercivity enhancement can be seen in all the cryo-milled samples. In the previous chapter, we have shown that the as cast and homogenized $Mn_{55}Bi_{45}$ alloy shows a H_C vale of 570 Oe and M_S and M_r values of 58.6 and 13 emu/g respectively. Also, 2 h cryo-milling of homogenized $Mn_{55}Bi_{45}$ alloy displayed a coercivity value of 6.7 kOe and M_S value of 32 emu/g [17]. This can be observed in the Fig. 5.10a. In addition, The kink observed in hysteresis loop (Fig 5.10a) is a characteristic feature for MnBi system obtained though milling route, arising from different particle sizes and chemical inhomogeneities [18]. The variation of magnetic properties of the nanocomposites can be seen in Figure 5.10b. The coercivity, M_S and M_r values of the nanocomposites with FeNi@C additions and thereby overall energy product of the system can be seen to be enhanced (Figure 5.10 b). The enhancement in magnetic properties are greater than that

obtained by rule of mixtures indicating the exchange coupling between the hard and soft magnetic phases. The best magnetic properties were obtained for the 15 wt.% FeNi@C addition and the observed values of M_S, H_C and M_r were 63 emu/g, 7.9 kOe and 38 emu/g respectively. The calculated energy product of the 15 wt.% addition nanocomposite with the optimum properties was 2.6 MGOe. The obtained energy product value was higher than the room temperature milled or cryo-milled MnBi samples. The value was even higher than MnBi/Fe_3C@C nanocomposites reported earlier in the previous chapter . As suggested earlier, the spin tunneling, through carbon might have aided the exchange coupling between MnBi and FeNi@C. Particularly, FeNi@C enhanced the composite's high initial magnetization, and the absence of oxide phases in the composites suggests that the carbon component also improved the composite's resistance to oxidation.

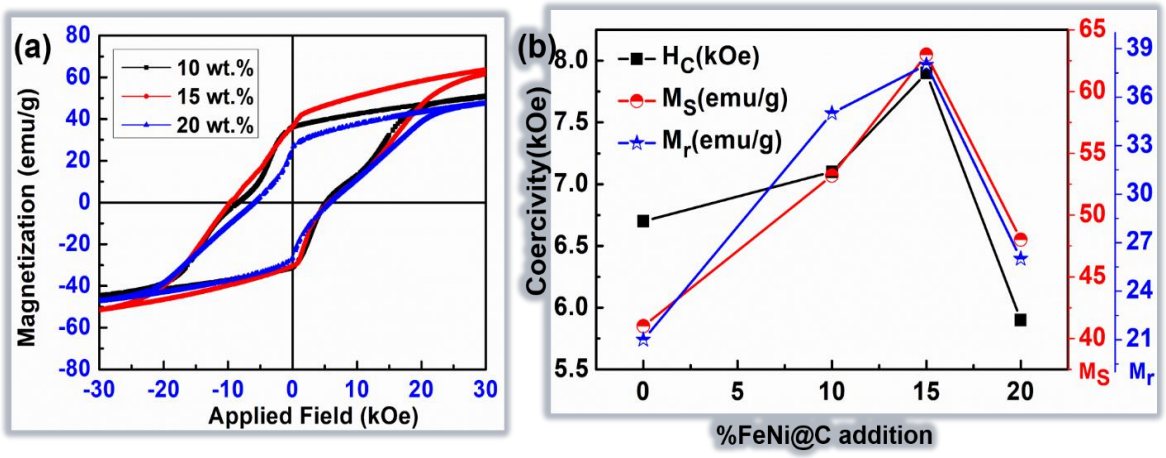

Figure 5.10. (a) M *vs*. H loops of the room temperature ball milled samples upto (± 30 kOe) and (b) variation of magnetic properties of cryo-milled nanocomposites with varying FeNi@C addition to $Mn_{55}Bi_{45}$.

Figure 5.11 displays the switching field distribution (SFD) curves of the nanocomposites. The degree of exchange coupling between the hard and soft components of the composite is qualitatively expressed by these SFD curves. Typically, a single, narrow peak in the dM/dH curve is related to the phases with small grain distribution and high exchange coupling [19]. The strong exchange interaction between the phases for the 15 wt.% sample can be corroborated by the single narrow peak obtained in the Figure 5.11. Whereas the 10 wt.% and 20 wt.% curves show broad loops in spite of being a single curve indicating the presence of improper exchange coupling.

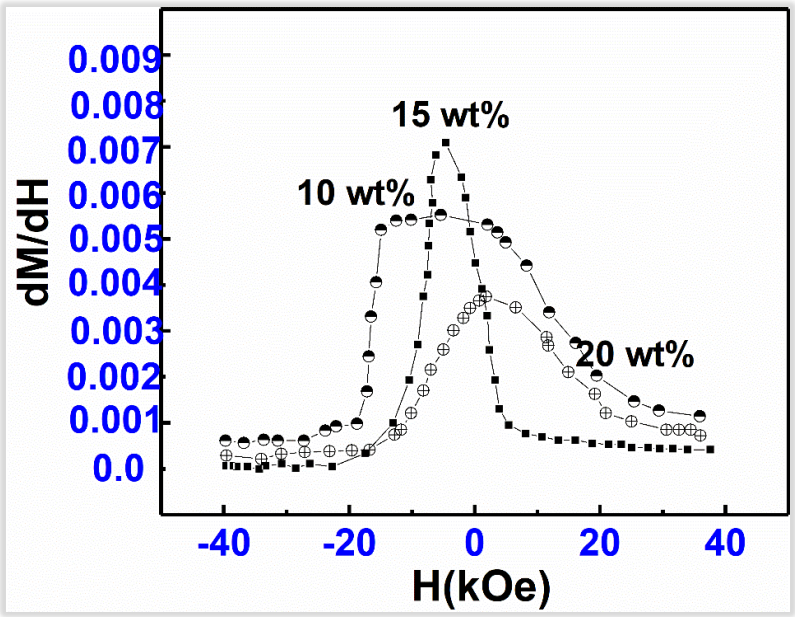

Figure 5.11. Switching field distribution curves of cryo-milled nanocomposites with 10, 15 and 20 wt.% FeNi@C addition.

In the present study, the obtained energy product value falls short of the desired one for the Gap magnet. This could be attributed to the isotropic nature of the particles obtained after milling. However, the energy product is considerably better than the earlier reports for isotropic particles [20]. Usually, these isotropic powders are subjected to magnetic field compaction followed by sintering to prepare bulk magnets. Therefore, the achieved values

may be enhanced by magnetic field annealing which introduces anisotropy along the field direction.

5.3. Conclusions:

Single phase and carbon coated FeNi nanoparticles were successfully synthesized using a simple hydrothermal technique, was confirmed through XRD and TEM measurements. These ferromagnetic nanoparticles displayed a relatively high saturation magnetization values (~147 emu/g), making it suitable as a soft-phase. Consequently, MnBi/FeNi@C nanocomposites, prepared by cryogenic-ball milling demonstrated superior hard magnetic properties. It was evident from the magnetic analysis of the cryo-milled composites that cryogenic temperature for milling and the addition of high magnetization soft phase improve the hard magnetic properties. Further, the best results were obtained for 15 wt. % addition of FeNi@C to MnBi with a H_C value of 7.9 kOe, M_S value of 63 emu/g, and M_r value of 38 emu/g. The results obtained in the present study surpass previous room temperature milling studies for isotropic particles and also our previously reported similar composites of MnBi/Fe_3C@C. These considerable enhancements in values suggest that sufficient coating of carbon onto the FeNi grains facilitated the exchange coupling between MnBi and FeNi. Thus, FeNi@C emerged as an attractive option, apart from the conventionally utilised Fe/FeCo phases as a soft magnetic phase, for the production of exchange-spring magnets.

5.4. References

1. B.K. Rai, S.R. Mishra, Magnetically enhanced hard–soft $SmCo_5$–FeNi composites obtained via high energy ball milling and heat treatment, J. Magn. Magn. Mater. 344 (2013) 211–216.
2. P. Scherrer, Bestimmung der Grosse und inneren Struktur von Kolloidteilchen mittels Rontgenstrahlen, Nach Ges Wiss Gottingen. 2 (1918) 8–100.
3. D. Han, N. Xiao, A promising broadband and thin microwave absorber based on ternary FeNi@ C@ polyaniline nanocomposites, RSC Adv. 5 (2015) 97944–97950.
4. A.Fan, C. Qin, X. Zhang, X. Yuan, S. Wang, X. Dai, Engineering FeNi alloy nanoparticles via synergistic ultralow Pt doping and nanocarbon capsulation for efficient hydrogen evolution, J. Mater. Chem. A. 7 (2019) 24347–24355.
5. J. Cui, J.-P. Choi, E. Polikarpov, M.J. Kramer, D. Johnson, Effect of composition and heat treatment on MnBi magnetic materials, Acta Mater. 79 (2014) 374–381.
6. W. Xie, E. Polikarpov, J.P. Choi, Effect of ball milling and heat treatment process on MnBi powders magnetic properties, J. Alloys Compd. 680 (2016) 1–5.
7. N.V.R. Rao, G.C. Hadjipanayis, Effect of process parameters on the phase formation, particle size and magnetic properties of MnBi nanoparticles prepared by mechanochemical synthesis, J. Alloys Compd. 616 (2014) 319–322.
8. N.S. Anuraag, S.K. Shaw, C. Upadhyay, N.K. Prasad, Mechanochemical synthesis of MnBi/Fe_3C@ C exchange coupled hard magnetic nanocomposites, J. Solid State Chem. 329 (2024) 124403.
9. V. Ly, X. Wu, Low-temperature phase MnBi compound: A potential candidate for rare-earth free permanent magnets, J. Alloys Compd. 615 (2014) S285–S290.

10. K. Jeet, V.K. Jindal, L.M. Bharadwaj, D.K. Avasthi, K. Dharamvir, Damaged carbon nanotubes get healed by ion irradiation, J. Appl. Phys. 108 (2010).
11. H.M. Kim, H.S. Kim, C.J. Lee, Morphological change of multiwalled carbon nanotubes through high-energy (MeV) ion irradiation, J. Appl. Phys. 97 (2005).
12. M.S. Dresselhaus, G. Dresselhaus, R. Saito, A. Jorio, Raman spectroscopy of carbon nanotubes, Phys. Rep. 409 (2005) 47–99.
13. R.J. Nemanich, S.A. Solin, First-and second-order Raman scattering from finite-size crystals of graphite, Phys. Rev. B. 20 (1979) 392.
14. R.N. Panda, N.S. Gajbhiye, Magnetic properties of nanocrystalline γ-Fe–Ni–N nitride systems, J. Appl. Phys. 86 (1999) 3295–3302.
15. T. Hayashi, S. Hirono, M. Tomita, S. Umemura, Magnetic thin films of cobalt nanocrystals encapsulated in graphite-like carbon, Nature. 381 (1996) 772–774.
16. A.Y. Yermakov, Structure and magnetic properties of carbon encapsulated FeCo@ C and FeNi@ C nanoparticles, Mater. Lett. 254 (2019) 202–205.
17. L. Zhen, Y.X. Gong, Electromagnetic properties of FeNi alloy nanoparticles prepared by hydrogen-thermal reduction method, J. Appl. Phys. 104 (2008).
18. N.V.R. Rao, A.M. Gabay, G.C. Hadjipanayis, Anisotropic fully dense MnBi permanent magnet with high energy product and high coercivity at elevated temperatures, J. Phys. D. Appl. Phys. 46 (2013) 62001.
19. H. Zeng, S. Sun, T.S. Vedantam, J.P. Liu, Z.-R. Dai, Z.-L. Wang, Exchange-coupled FePt nanoparticle assembly, Appl. Phys. Lett. 80 (2002) 2583–2585.
20. N.V.R. Rao, A.M. Gabay, Nanostructured bulk MnBi magnets fabricated by hot compaction of cryomilled powders, J. Phys. D. Appl. Phys. 46 (2013) 265001.